CHALMERS
UNIVERSITY OF TECHNOLOGY

Estimation of Apparent Inductances in Electrically Excited Synchronous Machines Using Enhanced Particle Swarm Optimization

Downloaded from: https://research.chalmers.se, 2026-04-16 03:05 UTC

Citation for the original published paper (version of record):
Jiang, B., Tang, J., Liu, Y. (2026). Estimation of Apparent Inductances in Electrically Excited Synchronous Machines Using Enhanced
Particle Swarm Optimization. IEEE Open Journal of the Industrial Electronics Society, In Press.
http://dx.doi.org/10.1109/OJIES.2026.3671359

N.B. When citing this work, cite the original published paper.

© 2026 IEEE. Personal use of this material is permitted. Permission from IEEE must be obtained for all other uses, in any current or future media, including reprinting/republishing this material for advertising or promotional purposes, or reuse of any copyrighted component of this work in other works.

(article starts on next page)

This article has been accepted for publication in IEEE Open Journal of the Industrial Electronics Society. This is the author's version which has not been fully edited and content may change prior to final publication. Citation information: DOI 10.1109/OJIES.2026.3671359

Date of publication xxxx 00, 0000, date of current version xxxx 00, 0000.
Digital Object Identifier XX.XXXX/YYY.20XX.ZZZZZZZ

Estimation of Apparent Inductances in Electrically Excited Synchronous Machines Using Enhanced Particle Swarm Optimization

Bowen Jiang[1], (Member, IEEE), Junfei Tang[2], (Member, IEEE) and Yujing Liu[1], (Senior Member, IEEE)
[1]Chalmers University of Technology, Gothenburg, Sweden
[2]Volvo Group, Gothenburg, Sweden

Corresponding author: Bowen Jiang (e-mail: bowen.jiang@chalmers.se).

This work was supported in part by the Swedish Electromobility Centre and Swedish Energy Agency.

ABSTRACT Electrically excited synchronous machines (EESMs) are becoming increasingly preferred in electric vehicles (EVs) due to their non-reliance on rare-earth materials. In traction EESMs, accurate estimation of apparent inductances is crucial for designing current controllers, calculating electromagnetic torques, and determining operation maps. Existing inductance estimation methods, developed based on the permanent magnet synchronous machines (PMSMs), only consider self inductances of the stator windings. However, due to the presence of both stator and field windings in EESMs, it is necessary to estimate both self and mutual inductances, which can greatly increase the estimation difficulty due to more unknown parameters. Hence, in this paper, a new EESM apparent inductance estimation method is proposed. In the proposed method, self and mutual inductances are simultaneously estimated using an enhanced particle swarm optimization (PSO) algorithm. The effectiveness of the proposed method is experimentally verified. Experimental results show that, compared to the standard PSO and dynamic PSO, the enhanced PSO exhibits higher estimation accuracy and better estimation stability. Additionally, by employing the estimated apparent inductances in the EESM current controller, precise current control can be achieved during dynamic processes.

INDEX TERMS Electrically excited synchronous machines (EESMs), electric vehicles (EVs), inductance estimation, particle swarm optimization (PSO)

I. INTRODUCTION

With the growing environmental consciousness among consumers and the enactment of supportive electrification policies by various countries, electric vehicles (EVs) have experienced rapid development in recent years [1][2]. As one of the fundamental components of EVs, electric machines (EMs) play a crucial role in shaping the performance of EVs [3]. Permanent magnet synchronous machines (PMSMs), owing to their high torque density and simple control, are presently the most commonly utilized EMs in EVs [4]. However, in PMSMs, the rotor flux is generated by permanent magnets, which are typically crafted from non-renewable rare-earth materials [5]. The extraction and refining processes of these materials can also be environmentally detrimental [6]. Moreover, permanent magnets also face the risk of being demagnetized under high temperature or high load conditions [7]. To avoid these issues, electrically excited synchronous machines (EESMs) are considered as a promising solution. In an EESM, the rotor flux is produced by injecting DC currents into the field winding, mitigating the use of permanent magnets [8]. In addition, compared to a PMSM, flexible rotor flux can be attained by regulating the field current, thereby allowing for higher power factor at high speeds and a broader flux-weakening range [9][10].

Accurately estimating the apparent inductances of EMs is crucial for several reasons. Firstly, these apparent inductances are used for calculating the feedforward voltages within the current controller, ensuring optimal dynamic performance of EMs. Moreover, precise estimation of electromagnetic torque output, which depends on accurate apparent inductance values, is imperative for effective control of vehicle dynamics [11]. Furthermore, when designing the machines' operation map,

This work is licensed under a Creative Commons Attribution 4.0 License. For more information, see https://creativecommons.org/licenses/by/4.0/

This article has been accepted for publication in IEEE Open Journal of the Industrial Electronics Society. This is the author's version which has not been fully edited and content may change prior to final publication. Citation information: DOI 10.1109/OJIES.2026.3671359

apparent inductances are essential in locating target operation points in accordance with specified control strategies, such as Maximum Torque Per Ampere (MTPA) [12].

Given their importance, various approaches have been proposed to determine the apparent inductances of EMs. The most straightforward method to determine the apparent inductances of EMs is by utilizing supplementary measuring equipment. For example, as detailed in [13], a signal generator produces sinusoidal voltages, which are then amplified before being applied to the stator windings. Analyzing the winding currents with a power analyzer allows for the determination of self inductances. However, in the context of EMs in EVs, the frequency and amplitude of the stator currents can exceed one thousand Hz and several hundred amperes at some operation points. Amplifiers face great challenges in generating voltages with amplitudes adequate for measuring apparent inductances at these operation points [14]. Moreover, the accuracy of these equipment may also impact the accuracy of inductance estimation. The finite element method (FEM) offers another relatively direct approach to obtaining apparent inductances of EMs [15]. FEM accounts for detailed geometries and material properties of laminations, allowing for precise modelling of saturation effects and inductance nonlinearity. Nevertheless, the high fidelity of FEM models leads to computationally-intensive calculations [16]. Additionally, manufacturing errors can also result in significant deviations between the actual machines' inductance values and those calculated by FEM. The Extended Kalman Filter (EKF), as is utilized in [17], can also address the nonlinearity of apparent inductances in EMs, providing precise estimation under high load conditions. However, in EESMs, when self and mutual inductances are both estimated, more states will be incorporated into the EKF state vector [18]. Consequently, the calculation of the Jacobian matrix within the EKF framework can become significantly intricate. To reduce calculation complexity, the Model Reference Adaptive System (MRAS) can also be employed to estimate the apparent inductances of EMs [19]. However, MRAS estimation accuracy is more susceptible to the quality of measurement. In addition, longer convergence periods are required, particularly when there are big initial estimation deviations [20]. The Recursive Least Squares (RLS) method demonstrates rapid convergence and less memory usage in estimating apparent inductances of EMs, yet its performance can be easily influenced by algorithmic settings, such as the forgetting factor and convergence criteria [21]. Methods based on Artificial Neural Networks (ANNs) have the advantage of bypassing the need for explicit electric models of EMs and giving estimation of apparent inductances solely based on measurable quantities. ANNs exhibit notable flexibility in handling inductance nonlinearity [22]. Nonetheless, the performance of ANNs depends on the availability of large training datasets and is also susceptible to overfitting issues.

Particle Swarm Optimization (PSO) is recognized as an attractive stochastic optimization method and is widely used in multiple parameter identification problems [23]. In terms of estimating inductances of EMs, PSO also demonstrates good performance owing to its ability to compute parallel. In [24], a standard PSO algorithm is applied to estimate the inductance and resistance of a PMSM by observing the d-axis current under single phase AC voltage input. In [25], it is illustrated that PSO can simultaneously estimate both the mechanical and electrical parameters of a PMSM by incorporating a rotation accelerating test. Additionally, PSO has also been hybridized with other algorithms, including the Gravitational Search Algorithm (GSA) [26] and Artificial Immune System (AIS) [27], resulting in improved performance in estimating EMs' inductances. However, in the aforementioned studies, PMSMs have been the primary focus of research. In PMSMs, the mutual inductances between the d-axis and q-axis are much smaller than the self inductances. Consequently, prior studies on electric machine parameter estimation have mainly targeted stator winding self inductances. In contrast, concerning EESMs, the mutual inductances between the stator and field windings are significant, which are crucial for current controller design. Despite their importance, no existing work has reported a method capable of simultaneously estimating the apparent self and mutual inductances of EESMs. Hence, the major objective of this paper is to address this research gap, with the main contributions summarized below:

- The apparent self and mutual inductances of EESMs are simultaneously estimated using a PSO-based method. By incorporating the estimated apparent inductances into the current controller, the transient current control performance is substantially improved.
- An enhanced PSO algorithm is developed, in which the weight factor, cognitive factor, and social factor are precisely designed and adjusted based on the collective behaviors of all searching particles. Compared with the standard PSO and dynamic PSO, the proposed enhanced PSO algorithm shows significantly improved estimation accuracy and estimation stability.
- A complete implementation procedure for applying the propose enhanced PSO algorithm to EESM inductance estimation is established. A local linearization approach that considers both stator and field current variations is introduced to handle magnetic saturation effects.

The rest of this paper is organized as follows. In section II, the EESM electrical model is first introduced. In section III, the proposed EESM apparent inductance estimator and the enhanced PSO algorithm are explained. In section IV, experimental results are discussed, before conclusions are drawn in section V.

This work is licensed under a Creative Commons Attribution 4.0 License. For more information, see https://creativecommons.org/licenses/by/4.0/

This article has been accepted for publication in IEEE Open Journal of the Industrial Electronics Society. This is the author's version which has not been fully edited and content may change prior to final publication. Citation information: DOI 10.1109/OJIES.2026.3671359

II. EESM ELECTRICAL MODEL

The EESM is modelled in the d&q frame, with the Clarke Transformation applied in the amplitude-invariant way. The EESM dynamic model can be formulated as:

$$\boldsymbol{u} = \boldsymbol{R}\cdot\boldsymbol{i} + \frac{d\boldsymbol{\psi}}{dt} + \boldsymbol{\omega}\cdot\boldsymbol{\psi}, \tag{1}$$

where $\boldsymbol{u}$ and $\boldsymbol{i}$ represent the voltage vector and current vector in the d-axis, q-axis, and field winding:

$$\boldsymbol{u} = \begin{bmatrix} u_\mathrm{d} \\ u_\mathrm{q} \\ u_\mathrm{f} \end{bmatrix}, \quad \boldsymbol{i} = \begin{bmatrix} i_\mathrm{d} \\ i_\mathrm{q} \\ i_\mathrm{f} \end{bmatrix}. \tag{2}$$

$\boldsymbol{R}$ is the resistance matrix, consisting of the stator winding resistance R_s and field winding resistance R_f:

$$\boldsymbol{R} = \begin{bmatrix} R_\mathrm{s} & 0 & 0 \\ 0 & R_\mathrm{s} & 0 \\ 0 & 0 & R_\mathrm{f} \end{bmatrix}. \tag{3}$$

$\boldsymbol{\omega}$ is the speed matrix, consisting of the rotor electrical rotating speed ω_r:

$$\boldsymbol{\omega} = \begin{bmatrix} 0 & -\omega_\mathrm{r} & 0 \\ \omega_\mathrm{r} & 0 & 0 \\ 0 & 0 & 0 \end{bmatrix}. \tag{4}$$

$\boldsymbol{\psi}$ represents the flux-linkage vector in the d-axis, q-axis, and field winding, and can be calculated by multiplying current vector and apparent inductance matrix $\boldsymbol{L}$:

$$\boldsymbol{\psi} = \begin{bmatrix} \psi_\mathrm{d} \\ \psi_\mathrm{q} \\ \psi_\mathrm{f} \end{bmatrix} = \boldsymbol{L}\cdot\boldsymbol{i} = \begin{bmatrix} L_\mathrm{dd} & L_\mathrm{dq} & L_\mathrm{df} \\ L_\mathrm{qd} & L_\mathrm{qq} & L_\mathrm{qf} \\ L_\mathrm{fd} & L_\mathrm{fq} & L_\mathrm{ff} \end{bmatrix} \cdot \begin{bmatrix} i_\mathrm{d} \\ i_\mathrm{q} \\ i_\mathrm{f} \end{bmatrix}. \tag{5}$$

The derivative of the flux-linkage in (1) can be computed by multiplying the derivative of the current vector with the incremental inductance matrix $\boldsymbol{l}$:

$$\frac{d\boldsymbol{\psi}}{dt} = \boldsymbol{l}\cdot\frac{d\boldsymbol{i}}{dt} = \begin{bmatrix} l_\mathrm{dd} & l_\mathrm{dq} & l_\mathrm{df} \\ l_\mathrm{qd} & l_\mathrm{qq} & l_\mathrm{qf} \\ l_\mathrm{fd} & l_\mathrm{fq} & l_\mathrm{ff} \end{bmatrix} \cdot \begin{bmatrix} \frac{di_\mathrm{d}}{dt} \\ \frac{di_\mathrm{q}}{dt} \\ \frac{di_\mathrm{f}}{dt} \end{bmatrix}. \tag{6}$$

Therefore, the EESM dynamic model described by (1) can be reformulated as:

$$\boldsymbol{u} = \boldsymbol{R}\cdot\boldsymbol{i} + \boldsymbol{l}\cdot\frac{d\boldsymbol{i}}{dt} + \boldsymbol{\omega}\cdot\boldsymbol{L}\cdot\boldsymbol{i}. \tag{7}$$

In steady-state, the current derivatives become zero. Hence, the EESM steady-state model becomes:

$$\boldsymbol{u} = \boldsymbol{R}\cdot\boldsymbol{i} + \boldsymbol{\omega}\cdot\boldsymbol{L}\cdot\boldsymbol{i}. \tag{8}$$

III. EESM APPARENT INDUCTANCE ESTIMATION

The EESM steady-state model described in (8) is utilized to estimate the values of EESM apparent inductances.

A. ESTIMATOR DESIGN

The steady-state voltages of the d-axis, q-axis, and the field winding can be obtained from (8):

$$u_\mathrm{d} = R_\mathrm{s}\cdot i_\mathrm{d} - \omega_\mathrm{r}\cdot\left(L_\mathrm{qd}\cdot i_\mathrm{d} + L_\mathrm{qq}\cdot i_\mathrm{q} + L_\mathrm{qf}\cdot i_\mathrm{f}\right), \tag{9}$$

$$u_\mathrm{q} = R_\mathrm{s}\cdot i_\mathrm{q} + \omega_\mathrm{r}\cdot\left(L_\mathrm{dd}\cdot i_\mathrm{d} + L_\mathrm{dq}\cdot i_\mathrm{q} + L_\mathrm{df}\cdot i_\mathrm{f}\right), \tag{10}$$

$$u_\mathrm{f} = R_\mathrm{f}\cdot i_\mathrm{f}. \tag{11}$$

Multiple unknown parameters are incorporated in (9), (10), and (11), but not all of them need to be estimated. Firstly, R_f can be directly calculated using (11). In addition, the mutual apparent inductances between the d-axis and q-axis can be ignored due to their substantially lower values in comparison to other apparent inductances:

$$L_\mathrm{dq} = L_\mathrm{qd} = 0. \tag{12}$$

Hence, five parameters, i.e., R_s, L_qq, L_qf, L_dd, L_df, shall be estimated. Due to flux saturation phenomena, altering any current within i_d, i_q, i_f leads to concurrent changes in the apparent inductances. This issue is addressed through local linearization. As is shown in Fig. 1, when one operation point is being studied, i.e., P_0: $\left(i_{\mathrm{d}0}, i_{\mathrm{q}0}, i_{\mathrm{f}0}\right)$, the apparent inductances are considered as constant within a small cubic area centered around the studied point. The lengths of the cubic area in three dimensions correspond to Δi_d, Δi_q and Δi_f. To further mitigate the effect of apparent inductance variations caused by current changes in different dimensions, the steady-state currents and voltages of eight operation points are employed to estimate the apparent inductances of P_0. These eight points correspond to the eight vertices of the studied cubic area, i.e.:, P_1, P_2, ... P_7, P_8, some of which are also shown in Fig. 1. The d-axis, q-axis, and field currents of these eight points are $\boldsymbol{i}_\mathbf{d}^\mathbf{m}$, $\boldsymbol{i}_\mathbf{q}^\mathbf{m}$, and $\boldsymbol{i}_\mathbf{f}^\mathbf{m}$:

$$\begin{aligned} \boldsymbol{i}_\mathbf{d}^\mathbf{m} &= [i_{\mathrm{d},1}^\mathrm{m}\ \ i_{\mathrm{d},2}^\mathrm{m}\ \ i_{\mathrm{d},3}^\mathrm{m}\ \ i_{\mathrm{d},4}^\mathrm{m}\ \ i_{\mathrm{d},5}^\mathrm{m}\ \ i_{\mathrm{d},6}^\mathrm{m}\ \ i_{\mathrm{d},7}^\mathrm{m}\ \ i_{\mathrm{d},8}^\mathrm{m}], \\ \boldsymbol{i}_\mathbf{q}^\mathbf{m} &= [i_{\mathrm{q},1}^\mathrm{m}\ \ i_{\mathrm{q},2}^\mathrm{m}\ \ i_{\mathrm{q},3}^\mathrm{m}\ \ i_{\mathrm{q},4}^\mathrm{m}\ \ i_{\mathrm{q},5}^\mathrm{m}\ \ i_{\mathrm{q},6}^\mathrm{m}\ \ i_{\mathrm{q},7}^\mathrm{m}\ \ i_{\mathrm{q},8}^\mathrm{m}], \\ \boldsymbol{i}_\mathbf{f}^\mathbf{m} &= [i_{\mathrm{f},1}^\mathrm{m}\ \ i_{\mathrm{f},2}^\mathrm{m}\ \ i_{\mathrm{f},3}^\mathrm{m}\ \ i_{\mathrm{f},4}^\mathrm{m}\ \ i_{\mathrm{f},5}^\mathrm{m}\ \ i_{\mathrm{f},6}^\mathrm{m}\ \ i_{\mathrm{f},7}^\mathrm{m}\ \ i_{\mathrm{f},8}^\mathrm{m}]. \end{aligned} \tag{13}$$

The d-axis and q-axis voltages of these eight points are $\boldsymbol{u}_\mathbf{d}^\mathbf{m}$ and $\boldsymbol{u}_\mathbf{q}^\mathbf{m}$:

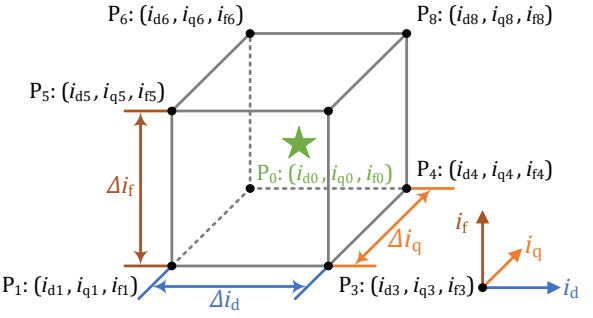

FIGURE 1. A cube containing the studied operation point.

This work is licensed under a Creative Commons Attribution 4.0 License. For more information, see https://creativecommons.org/licenses/by/4.0/

This article has been accepted for publication in IEEE Open Journal of the Industrial Electronics Society. This is the author's version which has not been fully edited and content may change prior to final publication. Citation information: DOI 10.1109/OJIES.2026.3671359

$$\boldsymbol{u}_{\mathbf{d}}^{\mathbf{m}} = [u_{\mathrm{d},1}^{\mathrm{m}}\ u_{\mathrm{d},2}^{\mathrm{m}}\ u_{\mathrm{d},3}^{\mathrm{m}}\ u_{\mathrm{d},4}^{\mathrm{m}}\ u_{\mathrm{d},5}^{\mathrm{m}}\ u_{\mathrm{d},6}^{\mathrm{m}}\ u_{\mathrm{d},7}^{\mathrm{m}}\ u_{\mathrm{d},8}^{\mathrm{m}}],$$
$$\boldsymbol{u}_{\mathbf{q}}^{\mathbf{m}} = [u_{\mathrm{q},1}^{\mathrm{m}}\ u_{\mathrm{q},2}^{\mathrm{m}}\ u_{\mathrm{q},3}^{\mathrm{m}}\ u_{\mathrm{q},4}^{\mathrm{m}}\ u_{\mathrm{q},5}^{\mathrm{m}}\ u_{\mathrm{q},6}^{\mathrm{m}}\ u_{\mathrm{q},7}^{\mathrm{m}}\ u_{\mathrm{q},8}^{\mathrm{m}}]. \quad (14)$$

Therefore, utilizing the steady-state currents and voltages of the eight points in (9) and (10) allows for the formulation of 16 equations. Hence, the apparent inductance estimation problem can be converted to an optimization problem, aiming to optimize the five unknown parameters to satisfy the 16 equations as closely as possible. The degree of satisfaction shall be quantified by a fitness function, which is designed as:

$$f(\hat{R}_{\mathrm{s}}, \hat{L}_{\mathrm{qq}}, \hat{L}_{\mathrm{qf}}, \hat{L}_{\mathrm{dd}}, \hat{L}_{\mathrm{df}}) = \sum_{\mathrm{j}=1}^{8} |\tilde{\boldsymbol{u}}_{\mathbf{d}}[\mathrm{j}]| + \sum_{\mathrm{j}=1}^{8} |\tilde{\boldsymbol{u}}_{\mathbf{q}}[\mathrm{j}]|, \quad (15)$$

where $\tilde{\boldsymbol{u}}_{\mathbf{d}}$ and $\tilde{\boldsymbol{u}}_{\mathbf{q}}$ are calculated as:

$$\tilde{\boldsymbol{u}}_{\mathbf{d}} = \boldsymbol{u}_{\mathbf{d}}^{\mathbf{m}} - \left(\hat{R}_{\mathrm{s}} \cdot \boldsymbol{i}_{\mathbf{d}}^{\mathbf{m}} - \omega_{\mathrm{r}} \cdot \left(\hat{L}_{\mathrm{qq}} \cdot \boldsymbol{i}_{\mathbf{q}}^{\mathbf{m}} + \hat{L}_{\mathrm{qf}} \cdot \boldsymbol{i}_{\mathbf{f}}^{\mathbf{m}}\right)\right), \quad (16)$$

$$\tilde{\boldsymbol{u}}_{\mathbf{q}} = \boldsymbol{u}_{\mathbf{q}}^{\mathbf{m}} - \left(\hat{R}_{\mathrm{s}} \cdot \boldsymbol{i}_{\mathbf{q}}^{\mathbf{m}} + \omega_{\mathrm{r}} \cdot \left(\hat{L}_{\mathrm{dd}} \cdot \boldsymbol{i}_{\mathbf{d}}^{\mathbf{m}} + \hat{L}_{\mathrm{df}} \cdot \boldsymbol{i}_{\mathbf{f}}^{\mathbf{m}}\right)\right), \quad (17)$$

where $\hat{R}_{\mathrm{s}}$, $\hat{L}_{\mathrm{qq}}$, $\hat{L}_{\mathrm{qf}}$, $\hat{L}_{\mathrm{dd}}$, $\hat{L}_{\mathrm{df}}$ are estimated parameters.

The schematic diagram of the EESM parameter estimator is illustrated in Fig. 2. The three-phase AC currents are measured and converted into the d&q currents, which, together with the measured field current, are sent to the current controller. In the current controller, the d-axis, q-axis, and field control voltages are calculated. The d&q control voltages determine the switching duty cycles of the three-phase inverter through Space Vector Pulse Width Modulation (SVPWM), while the field control voltage is sent to the excitation system, ensuring proper voltage is applied to the field winding. As is mentioned,

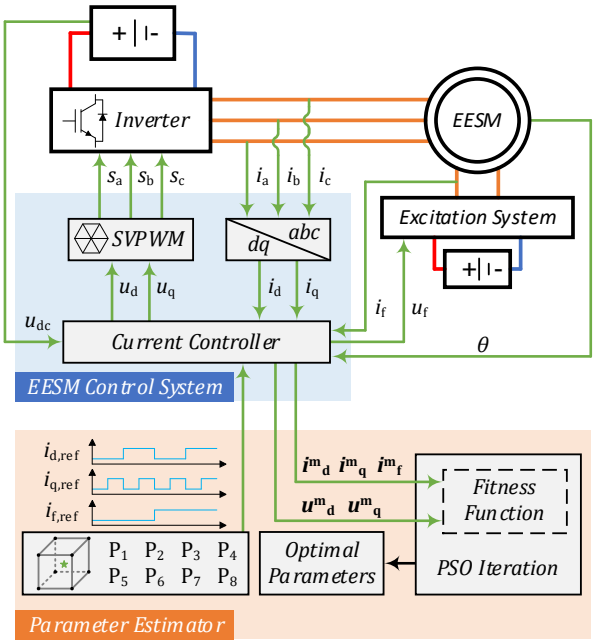

FIGURE 2. Schematic diagram of the EESM parameter estimator.

the parameter estimation of one operation point is based on its eight surrounding points. Therefore, these eight points form a testing cycle that serves as the reference current inputs to the current controller. In each PSO iteration, the steady-state control voltages obtained in the current controller and the steady-state measured currents are used for the fitness function calculation according to (15). The optimal parameters can be identified when the fitness function calculation converges.

It should be noted that when apparent inductances of many operation points need estimating, any vertex of each cube is also a vertex of other seven cubes. Therefore, the steady-state current and voltage of each vertex in a cube can be utilized for parameter estimation of all its eight surrounding points under study. Consequently, when employing the proposed estimator for grid-based parameter estimation, the required number of vertices to be tested will equal the number of operating points to be estimated.

In addition, the proposed method is currently implemented as an offline inductance estimation approach, meaning that the required current and voltage data should be measured in advance before being used in the estimator. This approach is well suited for EESM parameter calibration and current controller design prior to the installation of the machines in electric vehicles. However, during actual operations of EESMs in electric vehicles, a large amount of current and voltage measurement data is continuously available. These data can be appropriately selected and processed to be utilized by the proposed estimator. Therefore, the proposed method also has the potential to be extended for online inductance estimation. This extension is particularly valuable considering that EESM inductances may vary over time due to aging effects. By recalibrating the EESM inductances after a certain operating period, accurate EESM control performance can be maintained.

B. ENHANCED PARTICLE SWARM OPTIMIZATION

PSO is a stochastic optimization method inspired by the social behavior of bird flocking or fish schooling. In PSO, multiple particles collaboratively explore a multidimensional search space by sharing information about their individual and global best positions, with the objective of minimizing a predefined fitness function. In this section, the development of the proposed enhanced PSO is presented in a structured way. First, the formulation of the standard PSO is introduced, including the definition of particle position and velocity vectors, as well as their update rules in each iteration. Then, the proposed enhanced PSO is described in detail, where collective behavior information from all particles is incorporated to redesign the velocity update mechanism. Finally, a complete flowchart is provided to illustrate the overall implementation procedure of the enhanced PSO.

During the particle searching process, N particles work in parallel. Each particle (e.g., particle n) is described by a velocity vector $\boldsymbol{v}_{\mathbf{n}}$ and a position vector $\boldsymbol{x}_{\mathbf{n}}$:

This work is licensed under a Creative Commons Attribution 4.0 License. For more information, see https://creativecommons.org/licenses/by/4.0/

This article has been accepted for publication in IEEE Open Journal of the Industrial Electronics Society. This is the author's version which has not been fully edited and content may change prior to final publication. Citation information: DOI 10.1109/OJIES.2026.3671359

$$\boldsymbol{v_n} = [v_{n,1} \quad v_{n,2} \quad \cdots\cdots \quad v_{n,M-1} \quad v_{n,M}], \tag{18}$$

$$\boldsymbol{x_n} = [x_{n,1} \quad x_{n,2} \quad \cdots\cdots \quad x_{n,M-1} \quad x_{n,M}], \tag{19}$$

where M demotes the length of two vectors, which equals the number of parameters to be optimized. During the iterative optimization process, all particles are moving in a M dimensional space until an optimal position is found.

The particle velocity is updated according to:

$$\begin{aligned} v_{n,m}[k+1] = {} & w \cdot v_{n,m}[k] \\ & + c_1 \cdot r_1 \cdot \left(x_{n,m}^{pb}[k] - x_{n,m}[k]\right) \\ & + c_2 \cdot r_2 \cdot \left(x_m^{gb}[k] - x_{n,m}[k]\right), \end{aligned} \tag{20}$$

where $v_{n,m}[k]$ is the k^{th} iteration's velocity of the particle n in the dimension m. w, c_1 and c_2 are weight factor, cognitive factor and social factor. r_1 and r_2 are two independent random numbers within $(0,1)$ to incorporate the stochastic nature of the method. $x_{n,m}^{pb}[k]$ is the historical best position of the particle n in the dimension m until the k^{th} iteration. $x_m^{gb}[k]$ is the global best position of all particles in the dimension m until the k^{th} iteration. In order to maintain the swarm coherent, the calculated velocity needs to be further restricted according to:

$$v_{n,m}[k+1] = \min\left(\left(x_m^{up} - x_m^{low}\right), v_{n,m}[k+1]\right), \tag{21}$$

$$v_{n,m}[k+1] = \max\left(\left(x_m^{low} - x_m^{up}\right), v_{n,m}[k+1]\right), \tag{22}$$

where x_m^{up} and x_m^{low} are the upper and lower boundary values of the particle position in the dimension m.

The particle position is updated according to:

$$x_{n,m}[k+1] = x_{n,m}[k] + v_{n,m}[k+1], \tag{23}$$

where $x_{n,m}[k]$ is the k^{th} iteration's position of the particle n in the dimension m. It should be noted that during the particle searching process, particles are allowed to move beyond the boundary defined by x_m^{up} and x_m^{low} in order to enhance global searching capability. This design improves the swarm diversity and reduces the risk of suboptimal convergence, particularly when the true optimal lies near or outside the predefined boundary. However, to avoid excessive movement, particle velocities are constrained based on x_m^{up} and x_m^{low}, as is described in (21) and (22). This means the maximum distance a particle can move in each iteration is restricted, which helps maintain search stability while still allowing particles to explore beyond the boundary.

As described in (20), the velocity update equation consists of three parts. The first part is the exploration component and represents the particles' confidence in their current velocities, facilitating the expansion of the search area and exploration in the space. The second part is the cognitive component which embodies each particle's individual thinking and motivates them to learn from their own experiences and move towards their personal best position. The third part is the social component which signifies the exchange of information among all particles and guides them towards the globally best-known position. The velocity update manner of one particle is also illustrated in Fig. 3.

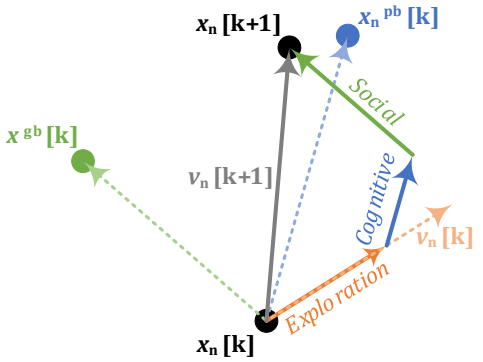

FIGURE 3. Illustration of one particle's velocity update manner.

In standard PSO, the values of w, c_1 and c_2 are constant throughout all iterations. However, as the particle swarm exhibits different distribution characteristics, the demands for three velocity update components (exploration, cognitive, and social components) also change. Therefore, an enhanced PSO algorithm is proposed in this paper, which has updated w, c_1 and c_2 in each iteration. In the proposed algorithm, the normalized distance square of each particle to the global best position $d_n[k]$ is calculated in every iteration:

$$d_n[k] = \sum_{m=1}^{M} \left(\left(x_{n,m}[k] - x_m^{gb}[k]\right)/\left(x_m^{max}[k] - x_m^{min}[k]\right)\right)^2, \tag{24}$$

where $x_m^{max}[k]$ and $x_m^{min}[k]$ are the maximum and minimum value of all particles in the dimension m until the k^{th} iteration.

At the beginning of the swarm search, all particles are highly scattered. During this stage, exploration and covering a wide search area are crucial to locate the global optimal region, requiring a larger w. Conversely, in the later stage of the swarm search, particles converge towards the optimal region. At this point, a smaller w should be used to achieve localized refinement of the optimal search. Hence, a factor describing the convergence degree of all particles is designed:

$$k_{con}[k] = e^{-\left(d_{avg}[k] - d_{min}[k]\right)}, \tag{25}$$

where $d_{avg}[k]$ and $d_{min}[k]$ represent the average value and minimum value of $d_n[k]$ $(n = 1,2,\ldots\ldots,N)$ in the k^{th} iteration. $k_{con}[k]$ is the convergence factor of all particles in the k^{th} iteration. As the iteration number increases, k_{con} increases and gradually approaches one. w is designed to be inversely correlated to k_{con}:

$$w[k] = w_{max} - (w_{max} - w_{min}) \cdot k_{con}[k], \tag{26}$$

This work is licensed under a Creative Commons Attribution 4.0 License. For more information, see https://creativecommons.org/licenses/by/4.0/

This article has been accepted for publication in IEEE Open Journal of the Industrial Electronics Society. This is the author's version which has not been fully edited and content may change prior to final publication. Citation information: DOI 10.1109/OJIES.2026.3671359

where $w[\mathrm{k}]$ is the weight factor in the k^{th} iteration. $w_{\max}$ and $w_{\min}$ are the maximum and minimum weight factors.

In addition to w, a judicious selection of c_1 and c_2 is also essential to achieve high optimization precision and rapid convergence speed. A larger c_1 can enhance the particles' global search ability, which is preferable in the initial optimization stage when particles are widely distributed. In contrast, a larger c_2 can expedite more particles' convergence towards the global optimal region, which is preferred in the later optimization stage when particles are gathering together. Therefore, a factor describing the dispersion level of all particles is designed:

$$k_{\mathrm{dis}}[\mathrm{k}] = \frac{d_{\mathrm{ave}}[\mathrm{k}] - d_{\min}[\mathrm{k}]}{d_{\max}[\mathrm{k}] - d_{\min}[\mathrm{k}]}, \tag{27}$$

where $d_{\max}[\mathrm{k}]$ denotes the maximum value of $d_{\mathrm{n}}[\mathrm{k}]$ $(\mathrm{n} = 1,2,\dots\dots,\mathrm{N})$ in the k^{th} iteration. $k_{\mathrm{dis}}[\mathrm{k}]$ is the dispersion factor of all particles in the k^{th} iteration. As the iteration number increases, k_{dis} decreases and gradually approaches zero. c_1 and c_2 are designed as:

$$c_1[\mathrm{k}] = c_{1,\mathrm{final}} + k_{\mathrm{dis}}[\mathrm{k}], \tag{28}$$

$$c_2[\mathrm{k}] = c_{2,\mathrm{final}} - k_{\mathrm{dis}}[\mathrm{k}], \tag{29}$$

where $c_1[\mathrm{k}]$ and $c_2[\mathrm{k}]$ are the cognitive and social factors in the k^{th} iteration. $c_{1,\mathrm{final}}$ and $c_{2,\mathrm{final}}$ are the approximate values that these two factors finally reach when particles have converged after a sufficient number of iterations.

Equations (25)-(29) define the convergence factor and dispersion factors, and their use in adjusting the weight factor, cognitive factor, and social factor in each particle searching iteration. These equations are original and also form the core concept of the proposed enhanced PSO.

The flow-chart of the proposed enhanced PSO algorithm is demonstrated in Fig. 4. Before the iteration starts, all particles are initialized by setting initial velocity and position values according to:

$$v_{\mathrm{n,m}}[0] = r_3 \cdot \left(x_{\mathrm{m}}^{\mathrm{up}} - x_{\mathrm{m}}^{\mathrm{low}}\right) - \frac{x_{\mathrm{m}}^{\mathrm{up}} - x_{\mathrm{m}}^{\mathrm{low}}}{2}, \tag{30}$$

$$x_{\mathrm{n,m}}[0] = r_4 \cdot \left(x_{\mathrm{m}}^{\mathrm{up}} - x_{\mathrm{m}}^{\mathrm{low}}\right) + x_{\mathrm{m}}^{\mathrm{low}}, \tag{31}$$

where $v_{\mathrm{n,m}}[0]$ and $x_{\mathrm{n,m}}[0]$ are the initial velocity and position of the particle n in the dimension m. r_3 and r_4 are two independent random numbers within $(0,1)$. Similarly, the historical best position of each particle and the global best position are also initialized according to (31). Within each iteration, w, c_1 and c_2 are firstly calculated according to (25)-(29). Subsequently, each particle is individually evaluated, where its fitness value is calculated according to (15). The calculated value is then compared with the fitness value of the particle's historical best position. If the particle's fitness value in the current iteration is lower, the particle's historical best position will be updated to its current position. Similarly, if the

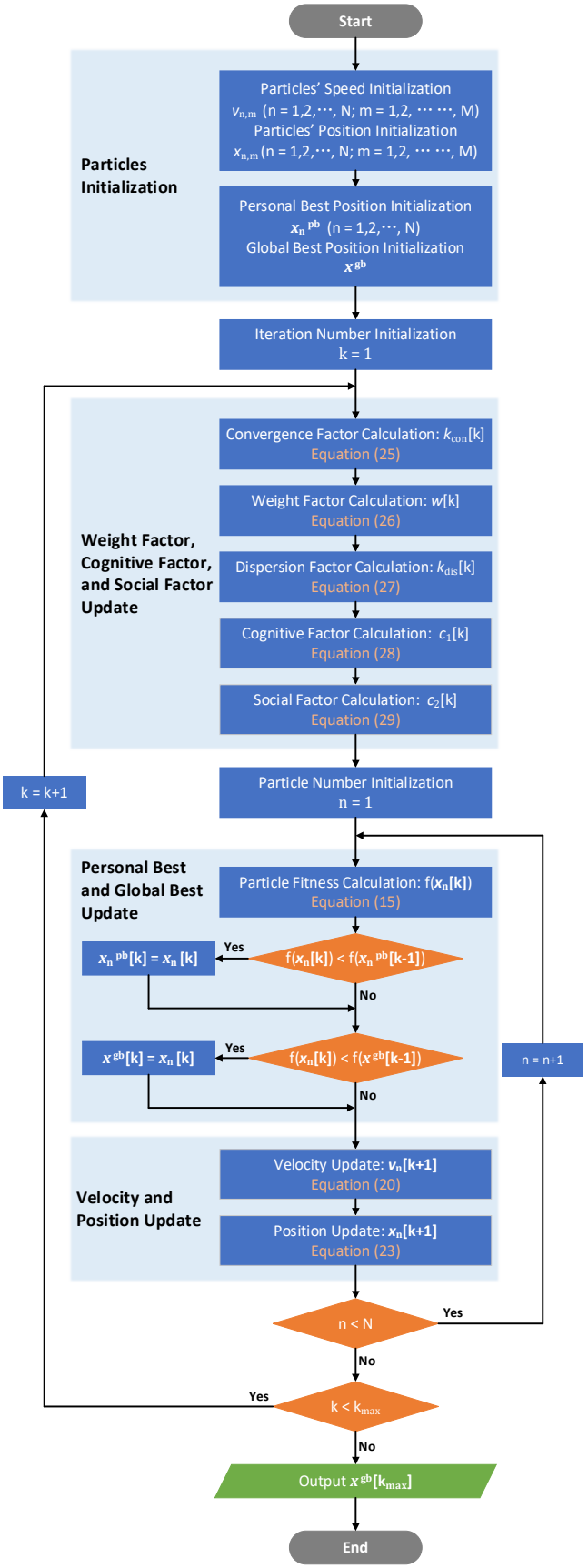

FIGURE 4. Flow-chart of the proposed enhanced PSO.

This work is licensed under a Creative Commons Attribution 4.0 License. For more information, see https://creativecommons.org/licenses/by/4.0/

This article has been accepted for publication in IEEE Open Journal of the Industrial Electronics Society. This is the author's version which has not been fully edited and content may change prior to final publication. Citation information: DOI 10.1109/OJIES.2026.3671359

particle's fitness value is even lower than the fitness value of the global best position, the global best position will also be updated to this particle's position in the current iteration. Afterwards, the velocity and position of the particle will be updated according to (20) and (23) respectively. One iteration finishes when all particles have been evaluated and updated. The iteration continues until the maximum iteration number is reached, and the global best position from the last iteration will be output, which is also the final optimization results.

IV. EXPERIMENTAL VERIFICATION

In order to verify the effectiveness of the proposed apparent inductance estimation method, a 60 kW EESM is prototyped, as is presented in Fig. 5. The prototyped EESM features three phases, four pole pairs, and 48 slots. The stator windings are made of hairpins, while the field winding is constructed using round wires. Detailed parameters of the prototyped EESM are listed in Table 1.

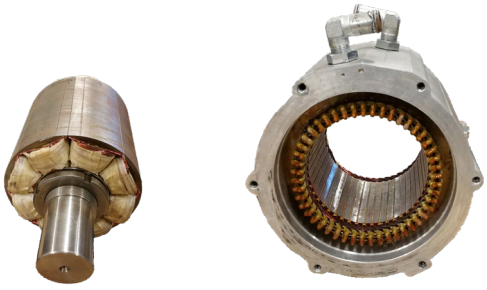

(a) Rotor (b) Stator

FIGURE 5. Rotor and stator of the EESM prototype.

TABLE 1. Parameters of the Prototyped EESM.

Parameter	Value	Unit
number of turns per pole in stator	4	-
number of turns per pole in rotor	112	-
stator inner diameter	123.0	mm
stator outer diameter	175.0	mm
rotor outer diameter	121.6	mm
lamination stack length	120.0	mm
base speed	2500	rpm
nominal DC-link voltage	360	V
peak power (30s)	60	kW
peak torque (30s)	190	Nm
shaft material	C45E	-
stator lamination material	B35AV1900	-
rotor lamination material	M235-35A	-

The test bench picture of the experimental setup is shown in Fig. 6. The prototyped EESM is back-to-back connected to a PMSM, which serves as a load machine. The stator currents of the EESM and PMSM are provided by two three-phase inverters. The field current of the EESM is provided by a brushless excitation system, which consists of an H-bridge inverter, a rotational transformer, and a rotational rectifier. During experimental tests, the PMSM functions as a generator and is controlled with a constant speed reference at -300 rpm (EESM rotates at 300 rpm). The EESM operates as a motor and is controlled with current reference inputs. The EESM stator currents are directly measured with current sensors. However, due to the design of brushless field excitation, the EESM field current is obtained through a telemetry system.

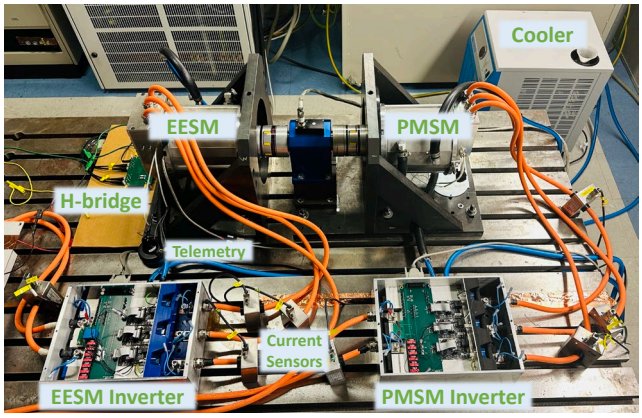

FIGURE 6. EESM and PMSM back-to-back test bench.

As is presented in Fig. 7, the dSPACE SCALEXIO system is employed as the controller for the PMSM and EESM. A dSPACE IO-board (dS6121) is utilized to receive current measurements from the test bench. By employing the measured currents, control voltages of the PMSM and EESM can be computed using field-oriented-control programs, which have been compiled into a dSPACE CPU-board (dS6001).

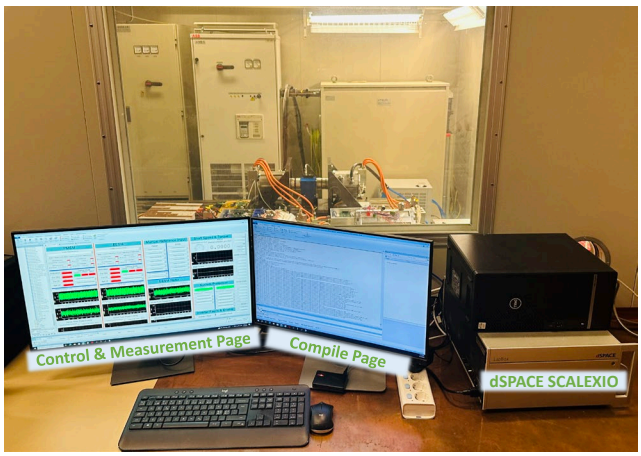

FIGURE 7. EESM and PMSM controller (dSPACE SCALEXIO).

A. EXPERIMENTAL DATA ACQUISITION

As is introduced in Section III-A, parameter estimation for a single operation point requires the steady-state currents and voltages collected at the eight vertices of a cubic area centered around the studied point. Here, the studied point is chosen under a low speed and load condition. The d-axis, q-axis, and field currents are specified to be -4A, 16A, and 1.5A. Under higher speed and load conditions, the d-axis and q-axis control

This work is licensed under a Creative Commons Attribution 4.0 License. For more information, see https://creativecommons.org/licenses/by/4.0/

This article has been accepted for publication in IEEE Open Journal of the Industrial Electronics Society. This is the author's version which has not been fully edited and content may change prior to final publication. Citation information: DOI 10.1109/OJIES.2026.3671359

voltages are expected to be higher according to (9) and (10). This leads to a higher signal-to-noise ratio, and the estimation accuracy is therefore expected to improve compared to the studied point presented in this paper. The lengths of the cubic area in three dimensions, i.e., Δi_{d}, Δi_{q}, and Δi_{f}, are set to be 4A, 4A, and 1A respectively. In Fig. 8 the experimental data of the eight vertices is presented. The stator and rotor currents are measured at a 10 kHz sampling rate. The d-axis and q-axis voltages are accessed from the EESM current controller, which are synchronously updated with the current measurement. From the obtained experimental data, it can be observed that the measured currents can follow the reference currents. However, when the reference currents step, it will take some time before the measured currents reach the next steady-state. Additionally, due to the unstable DC power supply used in the experimental setup, low-frequency fluctuations are observed in the voltage data. In order to mitigate the impact of these factors on parameter estimation, at each operation point, the reference currents are maintained unchanged for 10 seconds. Furthermore, the data from the middle 8 seconds are averaged to represent the steady-state current and voltage values.

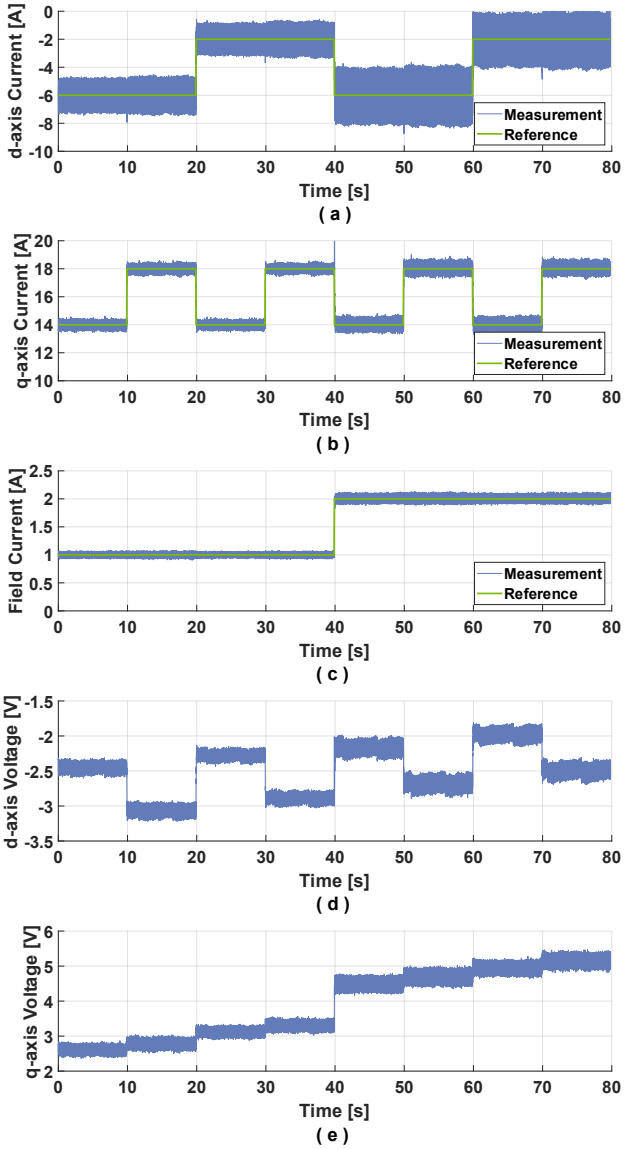

FIGURE 8. Experimental data of eight operation points at eight vertices within a cubic area (a) d-axis current (b) q-axis current (c) field current (d) d-axis voltage (e) q-axis voltage.

B. APPARENT INDUCTANCE ESTIMATION RESULTS

Utilizing the steady-state measurement, the enhanced PSO algorithm introduced in Section III-B is employed to estimate the EESM parameters. The unknown parameters include $\hat{R}_{\mathrm{s}}$, $\hat{L}_{\mathrm{qq}}$, $\hat{L}_{\mathrm{qf}}$, $\hat{L}_{\mathrm{dd}}$, $\hat{L}_{\mathrm{df}}$. Accordingly, M in (18) and (19) equals five. Regarding the selection of swarm size, an insufficient number of particles may lead to inadequate convergence of the search space, whereas an excessively large swarm can increase the computational burden without improving estimation performance. Therefore, the number of particles is usually selected by considering the dimensionality and complexity of the optimization problem. In the present study, the parameter estimation is performed in a five dimensional search space. A moderate swarm size is generally sufficient to ensure adequate exploitation while maintaining computational efficiency. Based on this consideration, a swarm size of 60 particles is selected. The maximum and minimum weight factors, i.e., $w_{\max}$ and $w_{\min}$ in (26), are set to be 1 and 0.5. The final cognitive and social factors, i.e., $c_{1,\mathrm{final}}$ and $c_{2,\mathrm{final}}$, are set to be 1.5 and 2.5. The initial guesses of the parameter are derived from finite element method (FEM) simulations. The upper and lower boundaries of the particle position are set to be symmetrically aligned with the parameter initial guesses with deviations of 50%, as is listed in Table 2.

TABLE 2. EESM Parameter Values (FEM Simulated & PSO Estimated).

Para-meter	FEM simulated	Lower boundary	Upper boundary	PSO estimated	Unit
$\hat{R}_{\mathrm{s}}$	75.00	37.50	112.5	86.62	mΩ
$\hat{L}_{\mathrm{qq}}$	1.416	0.708	2.124	1.297	mH
$\hat{L}_{\mathrm{qf}}$	-2.137	-3.206	-1.069	-2.511	mH
$\hat{L}_{\mathrm{dd}}$	1.415	0.706	2.123	0.9012	mH
$\hat{L}_{\mathrm{df}}$	23.79	11.90	35.69	15.71	mH

The optimization process of the proposed enhanced PSO is presented in Fig. 9. The convergence factor k_{con} calculated according to (25) is plotted in In Fig. 9a. k_{con} describes the degree of concentration of all particles relative to the global best position. In the beginning, the initial random distribution of all the particles results in a smaller k_{con}. Afterwards, k_{con} starts to increase. However, between the 5th iteration and the 10th iteration, a slight drop of k_{con} can be observed, which is caused by the significant changes of the global best position in the initial several iterations. Afterwards, k_{con} continues to increase and gradually approach one. This indicates that all particles are gathering toward the global best position and

This work is licensed under a Creative Commons Attribution 4.0 License. For more information, see https://creativecommons.org/licenses/by/4.0/

This article has been accepted for publication in IEEE Open Journal of the Industrial Electronics Society. This is the author's version which has not been fully edited and content may change prior to final publication. Citation information: DOI 10.1109/OJIES.2026.3671359

conducting more detailed searching. According to (26), the weight factor w is negatively correlated with k_{con}, which can be observed in Fig. 9b. The decreasing w is beneficial for balancing the global exploration in the initial iterations and the local exploitation in the later iterations. In Fig. 9c, the dispersion factor k_{dis} calculated according to (27) is plotted. The trend of k_{dis} also proves that particles disperse initially and converge with the increasing iteration number. The cognitive factor c_1 and social factor c_2 are presented in Fig. 9d. It can be observed that c_1 decreases while c_2 increases to their corresponding finial values, which is in accordance with (28) and (29). The fitness value of the global best position is shown in Fig. 9e. The rapid decrease in the fitness value at the beginning is attributed to the continuous discovery of better positions by different particles. After 15 iterations, the fitness value starts to decrease slowly and finally converges within 40 iterations. The five estimated parameters are represented by the five dimensions of the global best position. The changing of the estimated parameters over iterations is illustrated in Fig. 10. Similar to the fitness value, all the five estimated parameters exhibit rapid changes in the first 15 iterations due to the global searching. Subsequently, local searching is performed before the final optimized solution is achieved. The estimated parameters are listed in Table 2.

The performance of the proposed enhanced PSO is further evaluated by comparing with a standard PSO and a dynamic PSO. In the standard PSO, the weight factor, cognitive factor, and social factor are fixed throughout the optimization. The dynamic PSO represents another advanced PSO variant, in which these factors vary during the iteration process, but the collective behaviors of all searching particles are not explicitly considered [28]. To ensure a fair comparison, all three PSO

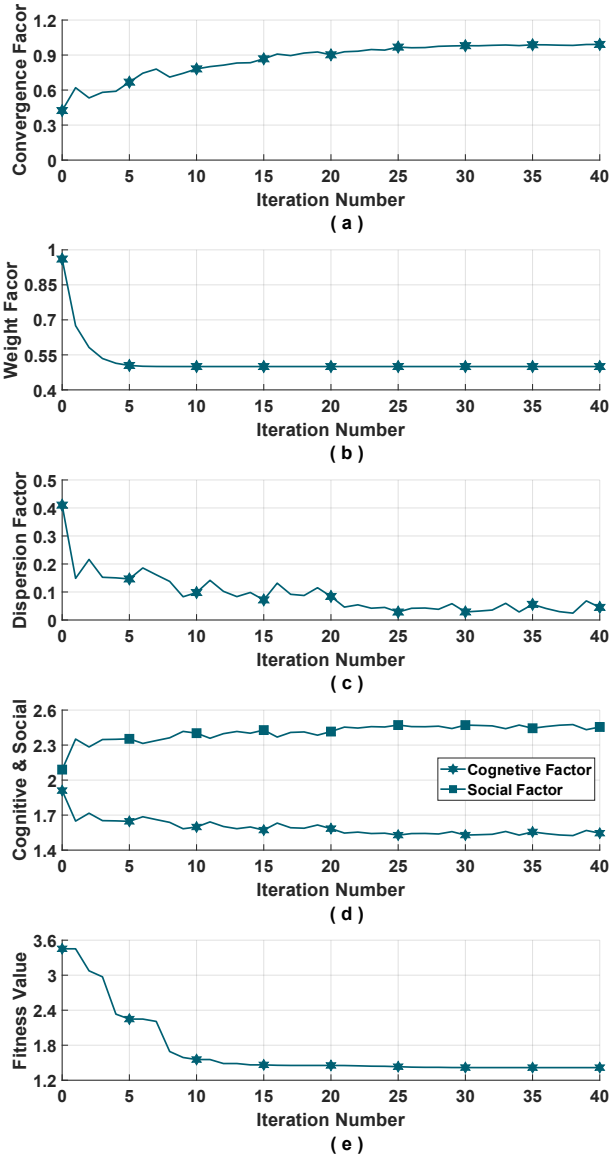

FIGURE 9. Optimization process of the proposed enhanced PSO (a) convergence factor k_{con} (b) weight factor w (c) dispersion factor k_{dis} (d) cognitive factor c_1 and social factors c_2 (e) fitness value.

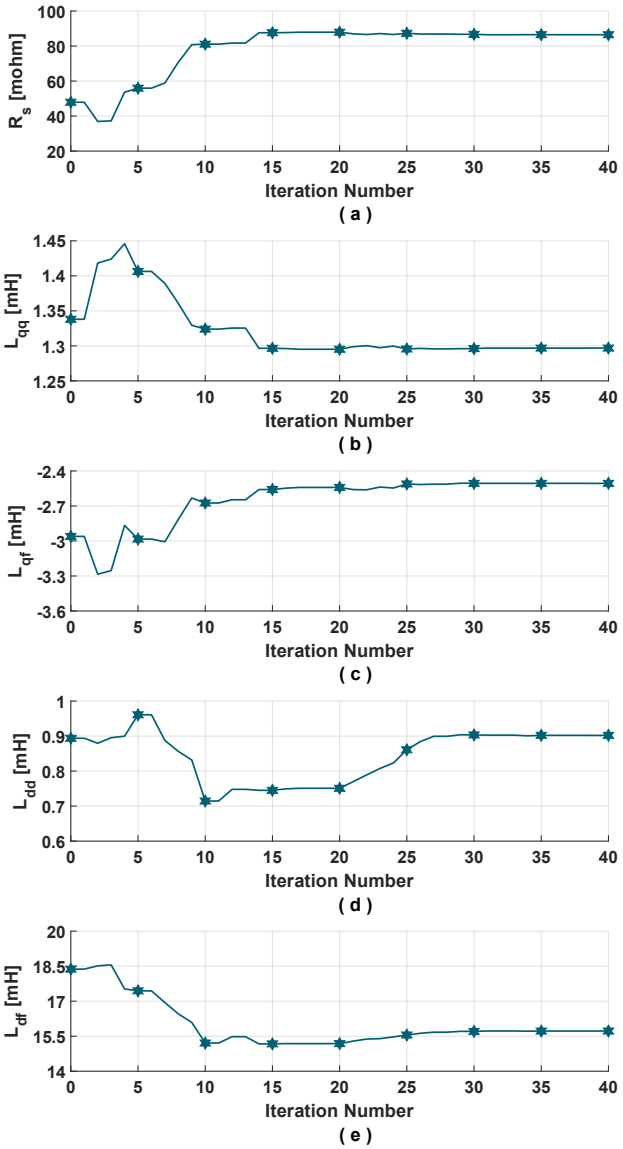

FIGURE 10. Estimated EESM parameters with increasing iteration number (a) R_{s} (b) L_{qq} (c) L_{qf} (d) L_{dd} (e) L_{df}.

This work is licensed under a Creative Commons Attribution 4.0 License. For more information, see https://creativecommons.org/licenses/by/4.0/

This article has been accepted for publication in IEEE Open Journal of the Industrial Electronics Society. This is the author's version which has not been fully edited and content may change prior to final publication. Citation information: DOI 10.1109/OJIES.2026.3671359

algorithms employ the same number of particles and the same maximum number of iterations for EESM parameter estimations. The evolution of the fitness values for the three PSO algorithms over iterations is compared in Fig. 11. Due to the random initialization of particle positions, the initial fitness values vary slightly among the three methods. However, it can be observed that the initial rapid decrease in fitness value requires more than 20 iterations for the standard PSO and dynamic PSO, whereas the enhanced PSO only needs less than 15 iterations. This improvement is due to the stronger global exploration capability of the enhanced PSO, which enables it to quickly identify the optimal region. Once the optimal region is located, the enhanced PSO also demonstrates better local exploitation, allowing the fitness value to continue decreasing. This indicates that the estimated parameters are further refined to achieve more accurate results. Compared with the standard PSO and dynamic PSO, the proposed enhanced PSO reduces the final fitness value by around 7.1% and 4.0% respectively.

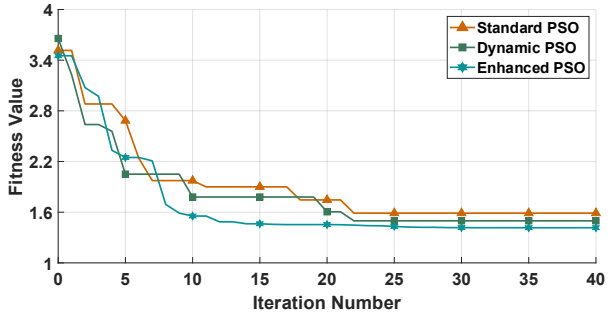

FIGURE 11. Fitness value evolution of the standard PSO, dynamic PSO, and proposed enhanced PSO.

In order to evaluate estimation stability, all three PSO algorithms are used to estimate the EESM parameters 20 times using identical experimental data. The converged fitness values and their corresponding probability density curves are presented in Fig. 12. It can be observed that the enhanced PSO achieves the lowest average converged fitness value, which further indicates its highest estimation accuracy among three PSO algorithms. Furthermore, the probability density curve for the enhanced PSO exhibits a much more concentrated distribution of the converged fitness values, demonstrating a significant improvement in estimation stability compared with the standard PSO and the dynamic PSO.

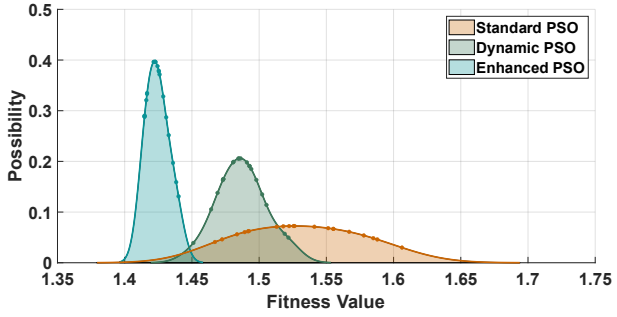

FIGURE 12. Converged fitness value distributions and the corresponding possibility density curves of the standard PSO, dynamic PSO, and proposed enhanced PSO.

C. EVALUATION OF ESTIMATED APPARENT INDUCTANCES

When the EESM runs under steady-state, inaccurate estimations of the apparent inductances in the current controller have little influence on machine performances as the PI-controller can adjust the control voltage so that the actual currents finally track the stable reference currents. However, during dynamic processes, when the reference currents are changing, incorrect transient control voltage may be applied due to inaccurate parameter estimations. The EESM apparent inductances are needed when designing the current controller on the d-axis and q-axis, as is illustrated in Fig. 13. Specifically, $\hat{L}_{\mathrm{qq}}$ and $\hat{L}_{\mathrm{qf}}$ are used for the d-axis control voltage calculation, while $\hat{L}_{\mathrm{dd}}$ and $\hat{L}_{\mathrm{df}}$ are used for the q-axis control voltage calculation. Therefore, in order to assess the accuracy of the parameter values estimated using the enhanced PSO, the estimated apparent inductances are incorporated into the current controller, and the machine is tested with a dynamic process. Additionally, parameter values obtained from the FEM simulations are also tested with the same dynamics process.

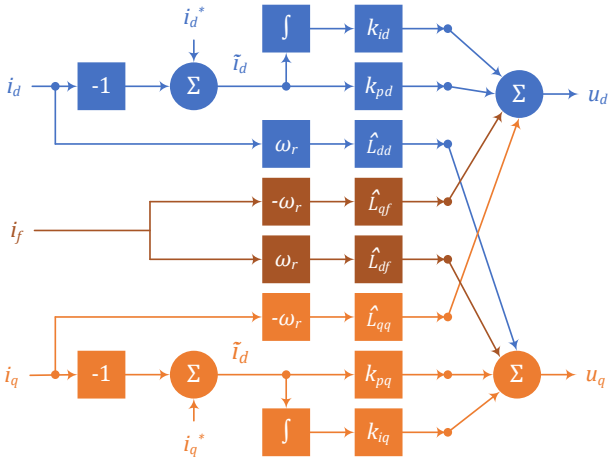

FIGURE 13. EESM current controller on the d-axis and q- axis.

Experimental results are presented in Fig. 14. Initially, the EESM runs under steady state with stable reference currents. At 0s, the references of the d-axis, q-axis, and field current simultaneously steps from -2A to -6A, from 18A to 14A and from 1A to 2A respectively, with a slew-rate of 300A/s. The d-axis control voltages are shown in Fig. 14d. It can be observed that the d-axis control voltage calculated using the PSO-estimated parameters is bigger than the one calculated using the FEM-simulated parameters during transients. This difference is due to that, as indicated in Table 2, the PSO-estimated $\hat{L}_{\mathrm{qq}}$ and $\hat{L}_{\mathrm{qf}}$ are smaller than the FEM-simulated values. According to Fig. 13, when the machine rotational speed is a positive value (300 rpm), the smaller $\hat{L}_{\mathrm{qq}}$ and $\hat{L}_{\mathrm{qf}}$ values in the current controller leads to a bigger d-axis control voltage. Similarly, in Fig. 14e, the smaller q-axis control voltage calculated using the PSO-estimated parameters is

This work is licensed under a Creative Commons Attribution 4.0 License. For more information, see https://creativecommons.org/licenses/by/4.0/

This article has been accepted for publication in IEEE Open Journal of the Industrial Electronics Society. This is the author's version which has not been fully edited and content may change prior to final publication. Citation information: DOI 10.1109/OJIES.2026.3671359

attributed to the smaller $\hat{L}_{dd}$ and $\hat{L}_{df}$ values estimated by the enhanced PSO. The resulting d-axis and q-axis currents are illustrated in Fig. 14a and Fig. 14b respectively. It can be observed that the d-axis current is not significantly affected by the variations of the apparent inductances in the current controller, which is due to the limited cross-coupling effect on the d-axis. However, a distinct difference is observed in the q-axis current. When the FEM-simulated apparent inductances are utilized in the current controller, the calculated control voltage is bigger than the required amount. Consequently, the q-axis current jumps from 18A to 20A when the transients start before decreasing to the new reference value at 14A. On the contrary, when the PSO-estimated apparent inductances are utilized in the current controller, the q-axis current closely tracks the reference value during the transients. Hence, the apparent inductances estimated by the enhanced PSO method are proved to be more accurate and are crucial for achieving precise current control during dynamic processes.

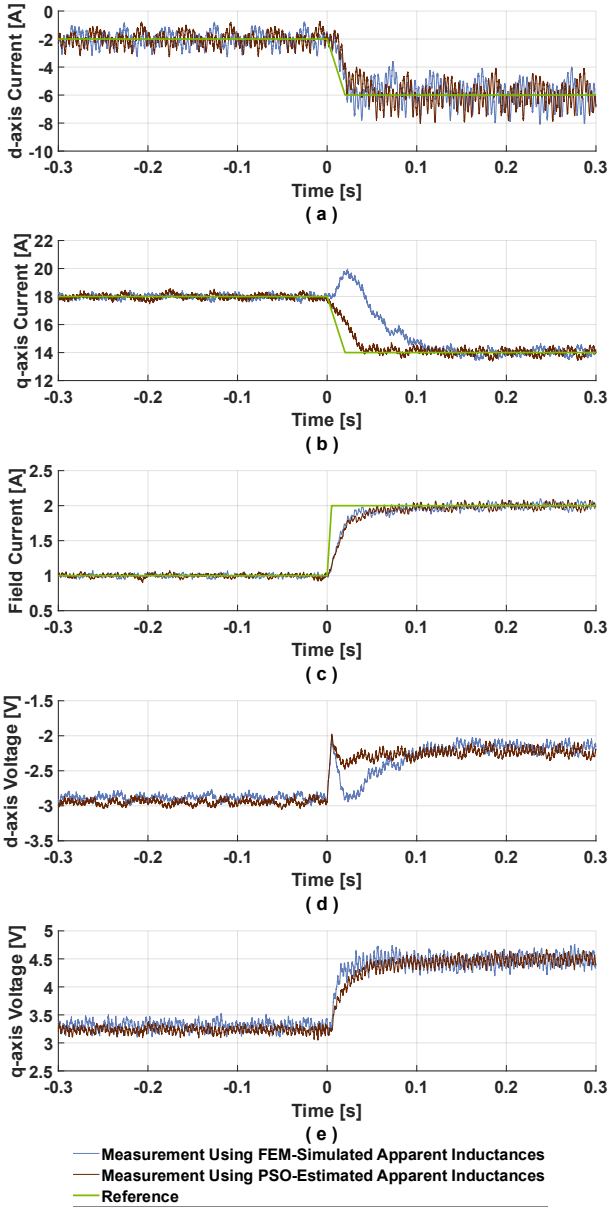

FIGURE 14. Dynamic process comparation between using the FEM-simulated apparent inductances and PSO-estimated apparent inductances in the current controller (a) d-axis current (b) q-axis current (c) field current (d) d-axis voltage (e) q-axis voltage.

V. CONCLUSIONS

In this paper, a new method is proposed to simultaneously estimate the apparent self and mutual inductances of EESMs. In the proposed method, an enhanced PSO algorithm is developed, which utilizes information on the collective behaviors of all particles to adaptively adjust the particle search trajectories in each iteration. The proposed method is experimentally verified. Compared with the standard PSO and the dynamic PSO, the proposed enhanced PSO can reduce the final converged fitness value by 7.1% and 4.0% respectively, demonstrating improved estimation accuracy. Moreover, repeated estimation tests also indicate that the proposed enhanced PSO exhibits better estimation stability. Finally, by employing the estimated apparent inductances in the EESM current controller, fast and accurate current control can be achieved during transient operation conditions.

REFERENCES

[1] I. Aghabali, J. Bauman, P. J. Kollmeyer, Y. Wang, B. Bilgin and A. Emadi, "800-V Electric Vehicle Powertrains: Review and Analysis of Benefits, Challenges, and Future Trends," in IEEE Transactions on Transportation Electrification, vol. 7, no. 3, pp. 927-948, Sept. 2021, doi: 10.1109/TTE.2020.3044938.

[2] B. Jiang, N. Sharma, Y. Liu, C. Li, and X. Huang, “Real-Time FPGA/CPU-Based Simulation of a Full-Electric Vehicle Integrated with a High-Fidelity Electric Drive Model,” Energies, vol. 15, no. 5, p. 1824, Mar. 2022, doi: 10.3390/en15051824.

[3] Z. Yang, F. Shang, I. P. Brown and M. Krishnamurthy, "Comparative Study of Interior Permanent Magnet, Induction, and Switched Reluctance Motor Drives for EV and HEV Applications," in IEEE Transactions on Transportation Electrification, vol. 1, no. 3, pp. 245-254, Oct. 2015, doi: 10.1109/TTE.2015.2470092.

[4] X. Liu, H. Chen, J. Zhao and A. Belahcen, "Research on the Performances and Parameters of Interior PMSM Used for Electric Vehicles," in IEEE Transactions on Industrial Electronics, vol. 63, no. 6, pp. 3533-3545, June 2016, doi: 10.1109/TIE.2016.2524415.

[5] J. D. Widmer, R. Martin and M. Kimiabeigi, "Electric Vehicle Traction Motors without Rare Earth Magnets," Sustainable Materials and Technologies, vol. 3, pp. 7-13, 2015.

[6] Y. Yang, A. Walton, R. Sheridan, K. Güth, R. Gauß, O. Gutfleisch, M. Buchert, B.-M. Steenari, T. V. Gerven, P. T. Jones and K. Binnemans, "REE Recovery from End-of-Life NdFeB Permanent Magnet Scrap: A Critical Review," Journal of Sustainable Metallurgy, vol. 3, no. 1, pp. 3 - 30, 2017.

[7] J. Faiz and H. Nejadi-Koti, "Demagnetization Fault Indexes in Permanent Magnet Synchronous Motors—An Overview," in IEEE Transactions on Magnetics, vol. 52, no. 4, pp. 1-11, April 2016, Art no. 8201511, doi: 10.1109/TMAG.2015.2480379.

[8] J. Tang, Y. Liu and N. Sharma, "Modeling and Experimental Verification of High-Frequency Inductive Brushless Exciter for Electrically Excited Synchronous Machines," in IEEE Transactions on Industry Applications, vol. 55, no. 5, pp. 4613-4623, Sept.-Oct. 2019, doi: 10.1109/TIA.2019.2921259.

[9] H. Chen, J. Tang, Y. Liu, B. Jiang and L. Boscaglia, "Electromagnetic Performance Investigation of a Brushless Electrically Excited Synchronous Machine for Long-Distance Heavy-Duty Electric Vehicles," in IEEE Transactions on Transportation Electrification, vol. 11, no. 1, pp. 225-235, Feb. 2025, doi: 10.1109/TTE.2024.3388430.

This work is licensed under a Creative Commons Attribution 4.0 License. For more information, see https://creativecommons.org/licenses/by/4.0/

This article has been accepted for publication in IEEE Open Journal of the Industrial Electronics Society. This is the author's version which has not been fully edited and content may change prior to final publication. Citation information: DOI 10.1109/OJIES.2026.3671359

[10] J. Tang, B. Jiang, L. Boscaglia, H. Chen and Y. Liu, "Observations of Field Current and Field Winding Temperature in Electrically Excited Synchronous Machines with Brushless Excitation," 2022 International Conference on Electrical Machines (ICEM), Valencia, Spain, 2022, pp. 841-847, doi: 10.1109/ICEM51905.2022.9910595.

[11] D. F. Alonso, Y. Kang, D. Fernández Laborda, M. M. Gómez, D. D. Reigosa and F. Briz, "Permanent Magnet Synchronous Machine Torque Estimation Using Low Cost Hall-Effect Sensors," in IEEE Transactions on Industry Applications, vol. 57, no. 4, pp. 3735-3743, July-Aug. 2021, doi: 10.1109/TIA.2021.3075924.

[12] H. Yang et al., "Investigation on Operating Characteristics of Asymmetric-Magnetic-Pole Interior Permanent Magnet Machines Under Maximum Torque Per Ampere Control," in IEEE Transactions on Industrial Electronics, vol. 72, no. 1, pp. 177-187, Jan. 2025, doi: 10.1109/TIE.2024.3409836.

[13] H. B. Ertan and İ. Şahin, "Evaluation of inductance measurement methods for PM machines," 2012 International Conference on Electrical Machines, Marseille, France, 2012, pp. 1672-1678, doi: 10.1109/ICElMach.2012.6350105.

[14] H. B. Ertan and I. Sahin, "Inductance Measurement Methods for Surface-Mount Permanent Magnet Machines," in IEEE Transactions on Instrumentation and Measurement, vol. 72, pp. 1-16, 2023, Art no. 2000116, doi: 10.1109/TIM.2022.3225048.

[15] Wang, Y., Yang, J., Deng, R. and Yang, G. (2020), Parameters estimation for multiphase induction machine with concentrated windings through finite element method. IET Electr. Power Appl., 14: 1807-1817. https://doi.org/10.1049/iet-epa.2019.0869.

[16] M. Tilahune, G. F. Olson, L. Peretti and M. Mamo, "Validation of FEM-Based Parameter Estimation for Variable Phase-Pole Induction Machines," in IEEE Transactions on Energy Conversion, vol. 38, no. 4, pp. 2310-2317, Dec. 2023, doi: 10.1109/TEC.2023.3272950.

[17] Z. Mynar, P. Vaclavek and P. Blaha, "Synchronous Reluctance Motor Parameter and State Estimation Using Extended Kalman Filter and Current Derivative Measurement," in IEEE Transactions on Industrial Electronics, vol. 68, no. 3, pp. 1972-1981, March 2021, doi: 10.1109/TIE.2020.2973897.

[18] W. Li, G. Feng, Z. Li, M. S. Toulabi and N. C. Kar, "Extended Kalman Filter Based Inductance Estimation for Dual Three-Phase Permanent Magnet Synchronous Motors Under the Single Open-Phase Fault," in IEEE Transactions on Energy Conversion, vol. 37, no. 2, pp. 1134-1144, June 2022, doi: 10.1109/TEC.2021.3129283.

[19] G. Pei, J. Liu, L. Li, P. Du, L. Pei and Y. Hu, "MRAS Based Online Parameter Identification for PMSM Considering VSI Nonlinearity," 2018 IEEE International Power Electronics and Application Conference and Exposition (PEAC), Shenzhen, China, 2018, pp. 1-7, doi: 10.1109/PEAC.2018.8590394.

[20] T. Boileau, N. Leboeuf, B. Nahid-Mobarakeh and F. Meibody-Tabar, "Online Identification of PMSM Parameters: Parameter Identifiability and Estimator Comparative Study," in IEEE Transactions on Industry Applications, vol. 47, no. 4, pp. 1944-1957, July-Aug. 2011, doi: 10.1109/TIA.2011.2155010.

[21] C. Lian, F. Xiao, J. Liu and S. Gao, "Parameter and VSI Nonlinearity Hybrid Estimation for PMSM Drives Based on Recursive Least Square," in IEEE Transactions on Transportation Electrification, vol. 9, no. 2, pp. 2195-2206, June 2023, doi: 10.1109/TTE.2022.3206606.

[22] Onursal Çetin, Adem Dalcalı, Feyzullah Temurtaş, "A comparative study on parameters estimation of squirrel cage induction motors using neural networks with unmemorized training," in Engineering Science and Technology, an International Journal, vol 23, Issue 5, Pages 1126-1133, 2020, ISSN 2215-0986, doi: 10.1016/j.jestch.2020.03.011.

[23] Z. -H. Zhan, J. Zhang, Y. Li and H. S. -H. Chung, "Adaptive Particle Swarm Optimization," in IEEE Transactions on Systems, Man, and Cybernetics, Part B (Cybernetics), vol. 39, no. 6, pp. 1362-1381, Dec. 2009, doi: 10.1109/TSMCB.2009.2015956.

[24] O. Sandre-Hernandez, R. Morales-Caporal, J. Rangel-Magdaleno, H. Peregrina-Barreto and J. N. Hernandez-Perez, "Parameter Identification of PMSMs Using Experimental Measurements and a PSO Algorithm," in IEEE Transactions on Instrumentation and Measurement, vol. 64, no. 8, pp. 2146-2154, Aug. 2015, doi: 10.1109/TIM.2015.2390958.

[25] Z. -H. Liu, H. -L. Wei, X. -H. Li, K. Liu and Q. -C. Zhong, "Global Identification of Electrical and Mechanical Parameters in PMSM Drive Based on Dynamic Self-Learning PSO," in IEEE Transactions on Power Electronics, vol. 33, no. 12, pp. 10858-10871, Dec. 2018, doi: 10.1109/TPEL.2018.2801331.

[26] Puri, V., Chauhan, Y.K. Offline parameter estimation of a modified permanent magnet generator using GSA and GSA-PSO. Soft Comput 26, 6333–6345 (2022). doi: 10.1007/s00500-021-06610-7.

[27] Z. -H. Liu, J. Zhang, S. -W. Zhou, X. -H. Li and K. Liu, "Coevolutionary Particle Swarm Optimization Using AIS and its Application in Multiparameter Estimation of PMSM," in IEEE Transactions on Cybernetics, vol. 43, no. 6, pp. 1921-1935, Dec. 2013, doi: 10.1109/TSMCB.2012.2235828.

[28] A. Zhou, X. Liu, D. Wu and J. Ge, "A Dynamic Particle Swarm Optimization Approach for Identifying Control Parameters of Virtual Synchronous Generators," 2025 4th International Conference on Energy and Electrical Power Systems (ICEEPS), Guangzhou, China, 2025, pp. 829-833, doi: 10.1109/ICEEPS66790.2025.11239720.

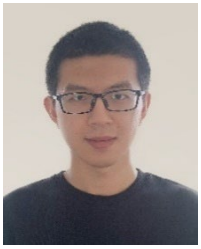

BOWEN JIANG received the M.Sc. degree in automotive engineering and Ph.D. degree in electric power engineering from Chalmers University of Technology, Gothenburg, Sweden, in 2020 and 2024 respectively. His research interests include parameter identification and dynamic control of electric machines.

JUNFEI TANG received the B.Eng. degree in electrical engineering from Jiangsu University, Zhenjiang, China, in 2013, and the M.Sc. and Ph.D. degrees in electric power engineering from Chalmers University of Technology, Gothenburg, Sweden, in 2016 and 2021 respectively. Now he works with Division of Electric Motor Systems at Volvo Group Trucks Technology, Gothenburg, Sweden.

YUJING LIU received the B.Sc., M.Sc., and Ph.D. degrees in electrical engineering from Harbin Institute of Technology, Harbin, China, in 1982, 1985, and 1988, respectively. In 1996–2013, he worked in ABB Corporate Research, Västerås, Sweden. Since 2013, he has been a professor of electrical power engineering with Chalmers University of Technology, Gothenburg, Sweden. His research interests include the research on motors, converters, and wireless charging for electric vehicles, generators and power electronics for tidal power conversion, and high efficiency machines for energy saving in industrial applications. Dr. Liu is a member in Swedish Standard Committee on Electrical Machines

This work is licensed under a Creative Commons Attribution 4.0 License. For more information, see https://creativecommons.org/licenses/by/4.0/